AIAA SciTech Forum
8-12 January 2024, Orlando, FL
AIAA SCITECH 2024 Forum

10.2514/6.2024-0592

# Numerical and experimental investigation of self excited thermoacoustic instabilities in a lean, partially premixed swirl flame

Michael Pries*, Andreas Fiolitakis†, Redjem Hadef‡ and Peter Gerlinger§
*German Aerospace Center (DLR), Institute of Combustion Technology, 70569 Stuttgart, Germany*
*Université Oum El Bouaghi, Département de Génie Mécanique, 04000 Oum El Bouaghi, Algeria*

**The computation of low Mach number self-excited thermoacoustic instabilities using large eddy simulations requires an efficient compressible, multi-species, reacting flow solver. Validation of such a method requires detailed experimental data covering the relevant flow and flame features. Difficulties may arise during the comparison of the numerical and experimental data, as both are subjected to inaccuracies. In this work, a well known lean, partially premixed swirl flame is used to demonstrate the excellent performance of the recently developed implicit characteristic splitting method for computing thermoacoustic instabilities. The swirl flame is also revisited experimentally with the focus to reduce inaccuracies of former experimental setups concerning the comparability with the numerical model. In this way, an excellent agreement is obtained between the numerical and experimental data concerning the acoustic frequencies as well as flame shapes. A subsequent analysis of the numerical data gives further insight in the thermoacoustical driving mechanisms as well as the nature of the acoustic eigenmodes.**



## I. Introduction

Environmental pollution through chemical emissions is a major design criterion developing modern combustion systems. The reduction of NOx- and CO-emissions leads to the design of lean premixed combustion chamber concepts prone to thermoacoustic instabilities. Such thermoacoustic instabilities must be avoided as they are associated with large pressure amplitudes capable to severely damage the combustion system. Ideally, a tendency to thermoacoustic instabilities is detected in the early phase of the design process by numerical methods. Unfortunately, correspondent simulations are highly complex and computational expensive. Different approaches have been followed. Large Eddy Simulation (LES) attempts to capture all relevant effects, but an efficient solver is needed capable of solving the compressible reacting balance equations at low Mach numbers. The classical approach using density as a primary variable has proven to be inefficient for low Mach number flows [1]. Main reasons are that the coupling between density and pressure becomes weak and the compressible system becomes stiff at the incompressible limit [2–5]. By the introduction of preconditioning these problems can be avoided [1, 6–13] but to ensure accuracy an iterative procedure is needed for each time step. Algorithms using pressure as a primary variable are primarily employed for the incompressible balance equations. An iterative procedure is often needed to ensure conservation of the variables. These methods have also been extended to compressible flows [14–22]. Splitting the balance equations into several subsystems is another approach solving the incompressible and compressible balance equations [23–25] where in general no iterative procedure is needed. Here, for mildly compressible flows the stiffness problem at low Mach numbers is frequently avoided by decomposing the balance equations based on the eigenvalues of the convective flux Jacobian matrix into an advective and non-advective subsystem [26–29]. The approach of [26] uses a semi-implicit scheme avoiding computationally expensive iterations and has enjoyed extensive usage in various fields. Among these are various reactive flow simulations [30–38] including spray flames [39–42], aeroacoustic and combustion noise simulations [43, 44] as well as simulations of combustion instabilities [45, 46]. In the current work a variant of the semi-implicit characteristic splitting scheme of [26] is employed, where the accuracy and stability of the method is improved as described in [47]. As the method is fully implicit it is called implicit characteristic splitting (ICS). The ICS scheme demonstrated its potential for generic benchmark problems, simple test cases as well as complex non-reactive

*Research Scientist, Institute of Combustion Technology, Computer Simulation Department
†Research Scientist, Institute of Combustion Technology, Computer Simulation Department
‡Research Scientist, Université Oum El Bouaghi, Département de Génie Mécanique
§Research Scientist, Institute of Combustion Technology, Computer Simulation Department

turbulent flows. What remains to be proven is the application towards self-excited thermoacoustic instabilities under realistic conditions.

A frequently used thermoacoustic test case is a model combustor derived from an industrial gas turbine burner designed by Turbomeca, featuring a lean methane/air swirl flame under atmospheric conditions. Depending on the operational point this combustor exhibits strong self-excited thermoacoustic pulsations as well as a precessing vortex core (PVC). Further, the combustor burns either with a detached M-shaped flame or an attached V-shaped flame. A *thermoacoustic pulsating* operational point (equivalence ratio $\phi = 0.7$, thermal power $P_{\mathrm{th}} = 25\,\mathrm{kW}$) of the burner is comprehensively investigated by means of pressure measurements as well as phase resolved measurements for OH* chemiluminescence, flow velocities, species concentration, and temperature [48–50]. There, a conical V-shaped flame is observed, while later on in [51] under marginally different conditions a flame with unpredictable transitions between an attached V-shaped flame and a detached M-shaped flame together with significant pressure amplitude variations is found. As the differences in the combustor setup and operational conditions of [51] are small compared to [48–50] this already demonstrates a high sensitivity of the considered swirl flame. In a later experimental study [52] the *thermoacoustic pulsating* operational point ($\phi = 0.7$, $P_{\mathrm{th}} = 25\,\mathrm{kW}$) has been revisited alongside an operational point burning at a richer equivalence ratio and a higher thermal power. Comparable to [51], the *thermoacoustic pulsating* operational point ($\phi = 0.7$, $P_{\mathrm{th}} = 25\,\mathrm{kW}$) in [52] is associated with an anchoring V-shaped flame whereas the second operational point burning at a richer equivalence ratio and higher thermal power exhibits an M-shaped flame and a lower sound pressure level. Further, in [52] a PVC structure is detected for the first time and only in the V-shaped flame. In all the studies mentioned so far (i. e. [48–52]) the fuel is injected into the air flow through a jet in crossflow configuration inside the swirler vanes resulting in a technically premixed configuration. Opposed to this, numerous studies exist in which the combustor is operated in a perfectly premixed configuration, where [53, 54] represent the most comprehensive studies. A detailed investigation of flame shapes and their dependence on equivalence ratio and thermal power is given in [54]. In contrast to [52], a PVC is detected in the lifted M-shaped flames. Additionally, the *thermoacoustic pulsating* operational point ($\phi = 0.7$, $P_{\mathrm{th}} = 25\,\mathrm{kW}$) investigated in [48–52] is re-assessed under perfectly premixed conditions where instead of the V-flame a stable M-flame is measured. Further, in [55] the influence of perfect and technical premixing is investigated for the operation point ($\phi = 0.9$, $P_{\mathrm{th}} = 25\,\mathrm{kW}$) considered there. It is found, that the overall flame features remain constant under technical and perfect premixing. This finding, together with the observations of [51] and [54] gives rise to the question, whether a detached M-shaped flame may also occur for the *thermoacoustic pulsating* operational point ($\phi = 0.7$, $P_{\mathrm{th}} = 25\,\mathrm{kW}$) under technical premixing for certain conditions.

The uncertainties of the *thermoacoustic pulsating* operational point ($\phi = 0.7$, $P_{\mathrm{th}} = 25\,\mathrm{kW}$) in flame shape and occurrence of the PVC to marginal differences in the experimental setup complicates numerical simulations. Usually, the numerical method relies on assumptions such as acoustically fully reflecting walls and a gas-proof combustor. In the experimental setup this is not the case as the combustion chamber is constructed using loosely fitted quartz glass windows held by metal posts. This contradicts the numerical modelling as loss of acoustical energy and also gaseous leakage occurs during the experimental runs. Examples for the implications of such effects are given in [56, 57] for a different swirl burner where strong transversal acoustic modes are present in the numerical results which are not observed in the experiments. According to [56] the origin of the transversal mode may lie in numerical artifacts, while the authors of [57] argue that acoustical imperfections and gaseous leakage in the experiment may damp the transversal mode observed in the simulation. In [57] the transversal mode is successfully damped by a partially reflecting wall boundary model. The relevance of the acoustical behaviour of the combustor walls is also displayed in [58] where a similar approach as in [57] is used to dampen transversal modes.

Despite these issues, and due to the extensive measurement data available, the *thermoacoustic pulsating* operational point ($\phi = 0.7$, $P_{\mathrm{th}} = 25\,\mathrm{kW}$) is an often used case to validate numerical methods with respect to self excited thermoacoustic instabilities [45, 59–67]. In this paper, new data are given in terms of pressure and OH* chemiluminescence measurements where the focus is upon preventing excessive loss of acoustical energy and gaseous leakage. This is achieved by using an all metal combustion chamber for the pressure measurements and a combustion chamber with a single optical port for the OH* chemiluminescence measurements.

## II. Numerical method

The balance equations for mass, momentum, energy, and the transport equations for species mass fractions are given by

$$\frac{\partial \rho}{\partial t} + \frac{\partial \rho u_i}{\partial x_i} = 0, \tag{1}$$

$$\frac{\partial \rho u_i}{\partial t} + \frac{\partial \rho u_i u_j}{\partial x_j} - \frac{\partial \tau_{ij}}{\partial x_j} + \frac{\partial p}{\partial x_i} = \rho f_i, \tag{2}$$

$$\frac{\partial \rho E}{\partial t} + \frac{\partial u_i \rho E}{\partial x_i} + \frac{\partial u_i p}{\partial x_i} - \frac{\partial u_j \tau_{ij}}{\partial x_i} + \frac{\partial q_i}{\partial x_i} = \rho u_i f_i + S_r, \tag{3}$$

$$\frac{\partial \rho Y_\alpha}{\partial t} + \frac{\partial \rho u_i Y_\alpha}{\partial x_i} + \frac{\partial j_{\alpha i}}{\partial x_i} = S_\alpha. \tag{4}$$

In Eqs. (1)-(4) and throughout this work the Einstein notation is used. Further, $x_i$ are the spatial coordinates, $t$ the physical time, $\rho$ the density, $u_i$ is the velocity vector, $p$ the pressure, $E$ is the specific total energy, and $Y_\alpha$ the species mass fraction for the component $\alpha$. The viscous stress tensor is defined by $\tau_{ij}$, the vector of the heat flux is given by $q_i$, and the diffusive mass flux is $j_{\alpha i}$. Radiative and chemical sources are given by $S_r$ and $S_\alpha$ whereas volume forces are denoted by $f_i$. The specific total energy is defined as the sum of the specific internal energy and the specific kinetic energy. A mixture of thermally perfect gases is assumed where the state equation for an ideal gas applies. The ICS scheme presented in [47] results in

$$\frac{\rho^* - \rho^n}{\Delta t} + \frac{\partial \rho u_i}{\partial x_i} - \rho \frac{\partial u_i}{\partial x_i} = 0, \tag{5}$$

$$\frac{\rho u_i^* - \rho u_i^n}{\Delta t} + \frac{\partial \rho u_i u_j}{\partial x_j} - \rho u_i \frac{\partial u_j}{\partial x_j} - \frac{\partial \tau_{ij}}{\partial x_j} = \rho f_i, \tag{6}$$

$$\frac{\rho E^* - \rho E^n}{\Delta t} + \frac{\partial \rho u_i E}{\partial x_i} - \rho E \frac{\partial u_i}{\partial x_i} - \frac{\partial u_j \tau_{ij}}{\partial x_i} + \frac{\partial q_i}{\partial x_i} = \rho u_i f_i + S_r, \tag{7}$$

$$\frac{\rho Y_\alpha^* - \rho Y_\alpha^n}{\Delta t} + \frac{\partial \rho u_i Y_\alpha}{\partial x_i} - \rho Y_\alpha \frac{\partial u_i}{\partial x_i} + \frac{\partial j_{\alpha i}}{\partial x_i} = S_\alpha \tag{8}$$

for the advective and

$$\frac{\rho^{n+1} - \rho^*}{\Delta t} - \frac{1}{c^2}\frac{\delta p}{\Delta t} = 0, \tag{9}$$

$$\frac{\rho u_i^{n+1} - \rho u_i^*}{\Delta t} - \frac{u_i}{c^2}\frac{\delta p}{\Delta t} + \frac{\partial}{\partial x_i}\left(\frac{p^* + p^{n+1}}{2}\right) = 0, \tag{10}$$

$$\frac{\rho E^{n+1} - \rho E^*}{\Delta t} - \frac{E}{c^2}\frac{\delta p}{\Delta t} + \frac{\partial}{\partial x_i}\left(\frac{u_i p^* + u_i p^{n+1}}{2}\right) = 0, \tag{11}$$

$$\frac{\rho Y_\alpha^{n+1} - \rho Y_\alpha^*}{\Delta t} - \frac{Y_\alpha}{c^2}\frac{\delta p}{\Delta t} = 0 \tag{12}$$

for the acoustic subsystems. In Eqs. (5)-(12), $c$ is the speed of sound, $\Delta t$ denotes the discrete time step size whereas $(\cdot)^n$ and $(\cdot)^{n+1}$ represent the current and next time levels whereas $(\cdot)^*$ denotes the intermediate solution. With $\delta p = p^{n+1} - p^*$ a pressure correction is introduced and the corresponding equation is given by

$$\begin{aligned} &\frac{\partial^2}{\partial x_i x_i}\delta p - \frac{\partial}{\partial x_i}\left(\frac{2u_i}{\Delta t c^2}\delta p\right) - \frac{4}{c^2 \Delta t^2}\delta p \\ &= -2\frac{\partial^2}{\partial x_i x_i} p^* + \frac{4}{\Delta t}\left(\frac{\rho^* + \rho^n}{2}\frac{\partial u_i^n}{\partial x_i}\right) \end{aligned} \tag{13}$$

as derived in [47]. Further, to prevent instabilities of the numerical solution, a stabilization term is introduced for the pressure update given by

$$p^{n+1} = p^* + \delta p + (1 - \psi(p))\kappa_2 \Delta^2 p + \kappa_4 \Delta^4 p, \tag{14}$$

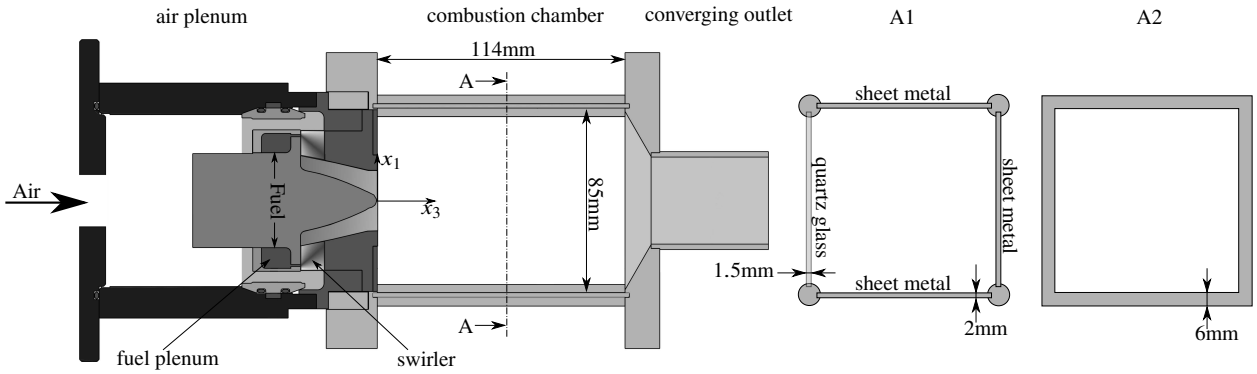


**Fig. 1 Schematic drawing of the investigated combustion device.**



where $\psi(p)$ is a limiter function based on pressure as defined in [68], $\kappa_2$ as well as $\kappa_4$ are case dependent coefficients, and $\Delta^2$ and $\Delta^4$ are diffusion operators of second and fourth order. For the LES simulation of the lean swirl burner, Eqs. (5)-(13) are used in their filtered form and discretized using a finite volume approach. The advective subsystem Eqs. (5)-(8) is discretized using a temporal second order implicit Crank Nicolson scheme. Application of an implicit instead of an explicit discretization increases the stability (which is especially beneficial for numerically stiff combustion problems) but leads to a nonlinear system of equations. Using the Newton Raphson scheme a fully implicit procedure for the advective subsystem is obtained. The pressure correction equation (Eq. (13)) is also discretized in a fully implicit manner. For the pressure correction variable $\delta p$, Dirichlet boundary conditions are applied at inflows and outflows whereas at walls von Neumann boundary conditions are used. Subsequent to solving the pressure correction equation the solution is advanced in an explicit manner using Eqs. (9)-(12) as well as the known pressure correction variable $\delta p$. A more detailed in depth description of the method is given in [47].

## III. Diagnostic techniques

**Pressure recording**

Pressure inside the combustion chamber and the air plenum is measured using remote microphone probes. They are equipped with B&K Type 4939 condenser microphones and are calibrated to recover the actual wall pressure inside the combustion device. A two-step calibration procedure according to [69–71] is applied, using an in house calibration device featuring an Visaton FR8 speaker. The pressure signals are recorded simultaneously by means of an A/D converter with an sampling rate of 100 kHz.

**Chemiluminescence imaging**

An intensified CMOS camera (LaVision HS-IRO/LaVision HSS8) equipped with a 64-mm focal length, f/2 UV lens and a bandpass filter (310-320 nm) by AHF is used to record the line-of-sight integrated OH* chemiluminescence signal emitted by the flame which acts as a marker for the heat release. The field of view covers the complete cross section of the combustion chamber. For different operational points the intensifiers gate time is kept constant while the gain is adjusted. To account for inaccuracies of the detector, a flat-field correction is applied to each frame. The frame rate of 15 kHz is also kept constant for all measurements. Alongside each camera recording a measurement of the combustion chamber pressure is made to provide each frame with a pressure value.

## IV. Experimental details and numerical modelling

A schematic drawing of the investigated combustion device is given in Fig. 1. The device in Fig. 1 is operated under atmospheric conditions in a technically premixed configuration. In the technically premixed configuration air and fuel are fed separately into the air and fuel plenum. Therefore, mixing takes place inside the twelve swirler vanes where the fuel is injected through a jet in crossflow configuration. The combustion chamber is mounted on top of the swirl burner and has a square cross section of 85x85 mm and a height of 114 mm. Experimentally, two different configurations are tested. Configuration A1 (cf. Fig. 1) utilizes the combustion chamber as used in [50] where the chamber side walls are

**Table 1 Investigated operational points**

| operational point | mass-flow air | mass-flow methane | thermal power | equivalence ratio |
|---|---|---|---|---|
| case 1 | 743 g/min | 30 g/min | 25 kW | 0.7 |
| case 2 | 650 g/min | 30 g/min | 25 kW | 0.8 |

**Table 2 Outflow parameters.**

| model parameter $\sigma$ | Mach number $Ma$ | characteristic length $l$ | target pressure $p_{\text{trgt}}$ |
|---|---|---|---|
| 0.58 | 0.05 | 0.114 m | 1 bar |



held by metal corner posts. As opposed to [50] in the new investigations only one side wall is equipped with a 1.5 mm thick quartz glass whereas the remaining three side walls are build of 2 mm thick sheet metal. Unlike the quartz glass the sheet metal inserts are tightly fit in order to reduce vibrations and gaseous leakage. To further reduce potential losses due to vibration of the side walls configuration A2 is used. Here, a separate combustion chamber is constructed out of 6 mm thick sheet metal walls which are welded together forming a gas-proof confinement. As no optical access is possible, configuration A2 is only used for pressure measurements. The flow rates of air and methane are controlled by Brooks Type 5853S mass-flow meters and monitored by Siemens Sitrans-FC MassFlo 2100 coriolis flowmeters. An overview of the considered operational points is given in Tab. 1 assuming an air composition of 23% oxygen mass fraction ($O_2$) and 77% nitrogen mass fraction ($N_2$). To provide a defined acoustic inlet boundary condition a choked orifice plate is used 45 mm upstream of the air plenum in the air supply line.

Considering the numerical aspects, the confined fluid domain of the device depicted in Fig. 1 is discretized by an unstructured grid of approximately ten million volumes. The ICS-scheme as described in Sec. II is used to compute the reactive flow of the operational points considered in Tab. 1, where a computational timestep of $0.1\mu s$ is used. Inflow and outflows are modelled by means of the Navier-Stokes characteristic boundary conditions (NSCBC) [72]. Comparable to the experiments, an acoustically fully reflective air inflow boundary with a constant mass-flow rate and a temperature of 320 K is chosen. Further, the inflow boundary to the fuel plenum is also considered to be acoustically fully reflective and a fuel temperature of 320 K is prescribed. For the combustor outflow a non reflective approach is chosen where the characteristic wave amplitude is prescribed according to [73] with the parameter set given in Tab. 2. The walls of the combustor are considered to be isothermal and acoustically fully reflective. A temperature of 320 K is prescribed at the walls of the air plenum, swirler, and fuel plenum. For the combustion chamber base plate wall a linear fit for the wall temperatures according to the measurement results given in [74] is used whereas the sidewall temperature is fit using a polynomial base function according to the findings in [75]. The temperatures of the walls connecting the swirler and the combustion chamber base plate are linearly interpolated. Further, the combustion processes are modeled using a finite-rate chemistry approach, where chemical kinetics are described by the DRM19 [76] mechanism. The WALE model [77] with a model constant $C_W = 0.4$ is used as a sub gird scale model for the LES and the filtered chemical source term is closed by means of an assumed probability density function [78] approach.

# V. Results

## A. Experimental findings

Selected time intervals of the pressure measurements as well as the corresponding phase space reconstruction from configuration A2 for case 1 and case 2 are displayed in Fig. 2 and Fig. 3. In case 1 as well as in case 2 the amplitude of the air plenum pressure is higher than that of the combustion chamber pressure. Moreover, the combustion chamber pressure of case 1 displays a pronounced double peak in the time signal where local maxima are found for $\Phi_3$ and $\Phi_7$. This is in accordance with the findings of prior measurements for case 1 given in [45]. The pronounced double peak of the combustion chamber pressure leads to the double loop attractor displayed in Fig. 2b. Additionally, a phase lag of less than $\pi$ can be observed between the pressure signals of the combustion chamber and the air plenum. Similar observations are made for case 2. Here, the phase lag is again less than $\pi$ but no pronounced second peak is observed at $\Phi_7$. In phase space (cf. Fig. 3b) a deformed single loop attractor is revealed. The corresponding power spectral densities

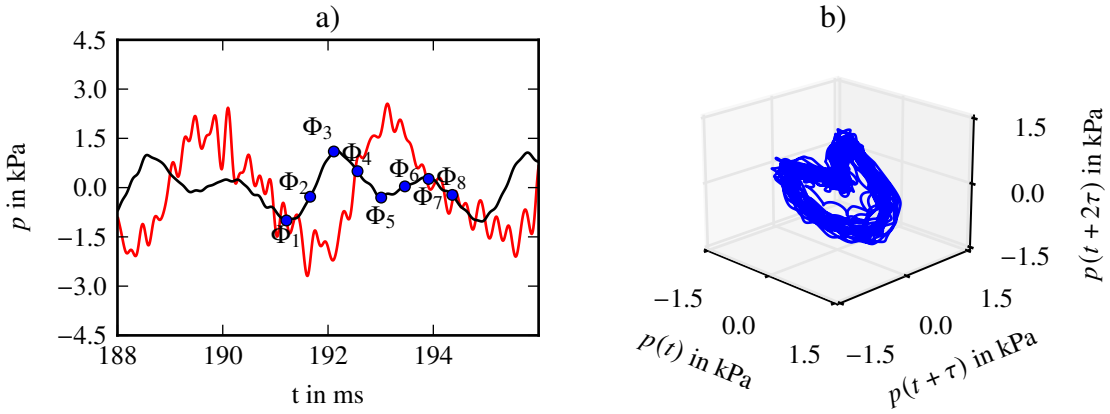


**Fig. 2 Selected time interval from the simultaneously measured pressure signal of configuration A2 and case 1. a) Pressure inside the air plenum (——), combustion chamber (——), and definition of phases ($\Phi_1$ to $\Phi_8$). b) combustion chamber pressure plotted in phase space** ($\tau = 0.56$ ms)

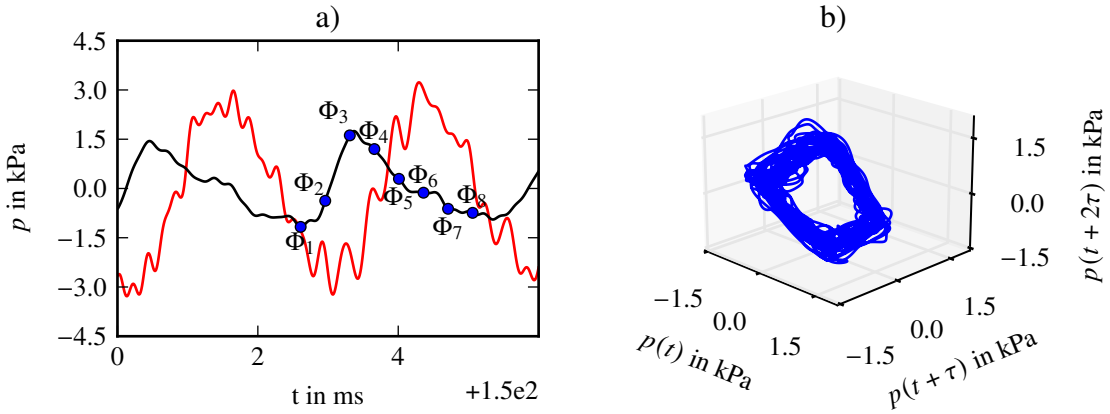


**Fig. 3 Selected time interval from the simultaneously measured pressure signal of configuration A2 and case 2. a) Pressure inside the air plenum (——), combustion chamber (——), and definition of phases ($\Phi_1$ to $\Phi_8$). b) combustion chamber pressure plotted in phase space** ($\tau = 0.66$ ms)

(PSDs) computed using Welchs method for case 1 and case 2 are displayed in Fig. 4. In Fig. 4a the PSD for case 1 alongside the PSDs measured with a combustion chamber equipped with quartz glass walls (cf. [45]) and sheet metal (cf. [45]) are given. Due to the new calibration method used, a frequency range up to 5000 Hz is available, revealing no prominent high frequency modes in the stiff combustion chamber configuration A2. Focusing on the first prominent peak, a slightly higher frequency for configuration A2 ($f_{\mathrm{A2}_1} = 284$ Hz) is found as compared to the measurements with quartz glass walls ($f_{\mathrm{glass}} = 276$ Hz) and sheet metal walls ($f_{\mathrm{metal}} = 274$ Hz). Considering the amplitudes, a same order of magnitude is observed using the configuration A2 as compared to the measurements with glass and sheet metal walls. As expected, the amplitudes of the peaks for configuration A2 and the sheet metal setup are higher than the amplitudes of the quartz glass setup. However, comparing the amplitudes of the peaks for configuration A2 and measurements with sheet metal, lower values are found for configuration A2. This unintuitive behaviour may either be attributed to the new calibration method used for configuration A2 or to the different probe design and usage of piezo-resistive sensors in the measurements of the sheet metal configuration (cf. [45]). Further, the measurements for configuration A2 reveal additional peaks at higher harmonic frequencies which have not been seen or at least were only slightly visible in prior measurement of case 1. Looking at Fig. 4b, the PSD of case 2 reveals a comparable power distribution as case 1. Again,

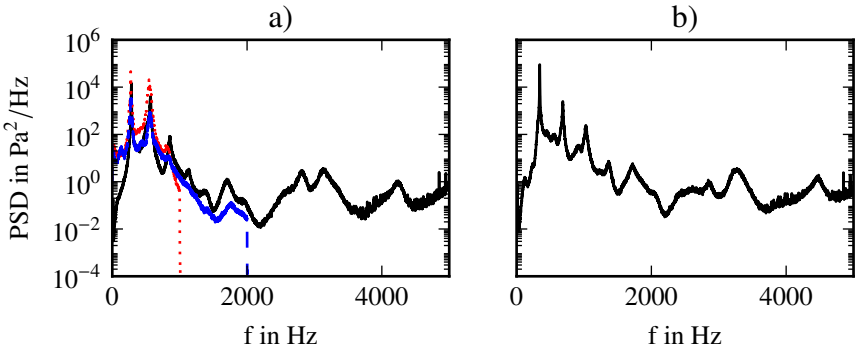


**Fig. 4 Computed power spectral density for the measured pressures inside the combustion chamber of configuration A2 for case 1 (a)) and case 2 (b)). (——) configuration A2 (·····) measurements with sheet metal walls [45] (- - -) measurements with quartz glass walls [45]**

three prominent peaks are visible whereby the first peak ($f_{A2_2}$ = 343 Hz) shows a higher frequency as compared to case 1 due to the richer regime and higher combustion chamber temperatures. Also the difference in amplitude between the first and second peak appears to be larger, leading to the deformed single loop attractor displayed in Fig. 3b. In Fig. 5 and Fig. 6 the phase averaged OH*-chemiluminescence measurements are displayed for configuration A1 of case 1 and case 2. The definition of each phase is based on the pressure inside the combustion chamber. This is exemplarily depicted for a single oscillation for configuration A2 in Fig. 2a (case 1) and Fig. 3a (case 2). The corresponding camera recordings obtained are then averaged and the signals are normalized. A comparability in between the signal intensities for the phases of each case is possible whereas no comparability is given in between case 1 and case 2. Considering the different phases, case 1 and case 2 show a similar pattern as largest amounts of OH* are detected for phases $\Phi_4$ to $\Phi_6$ with a maximum at $\Phi_5$. However, the shapes differ between case 1 and case 2. For case 1 no OH* is detected close to the swirl injector whereas significant amounts are detected for case 2. As OH*-chemiluminescence acts as a marker for heat release, a detached flame is observed for case 1 and an attached flame for case 2.

### B. Numerical findings

*Comparison against measurement data*

Time intervals for the computed pressure inside the combustion chamber and the air plenum are given in Fig. 7 for case 1 and in Fig. 8 for case 2. As observed for the measurements (Fig. 2 and Fig. 3), for both cases, the pressure amplitude in the air plenum is larger than the pressure amplitude inside the combustion chamber. Additionally, the pressure amplitudes are overpredicted for the computed results as compared to the measurements. Further, the pronounced double peak for the combustion chamber pressure of case 1 is not observed for the computed results. However, in frequency space an overall good agreement is obtained for case 1 as displayed in Fig. 9 and for case 2 displayed in Fig. 10. While for case 1 the amplitude of the first peak is slightly overpredicted, the frequencies match perfectly. Additionally the difference in amplitude between the first two peaks for case 1 is larger than for the measurements which explains the missing double peak in the pressure signal of Fig. 7. For case 2 the amplitudes of the peaks are in a good agreement but the frequencies deviate slightly from the measurements. As for the OH*-chemiluminescence measurements a phase averaging is performed based on the computed results. Here, instead of the OH*-chemiluminescence the line of sight integrated heat release is averaged. The averaging procedure is the same as for the experiments and the phase locations are displayed for a single oscillation in Fig. 7 for case 1 and Fig. 8 for case 2. The phase averaged heat release of case 1 is given by Fig. 11 and of case 2 by Fig. 12. Again, a good agreement as compared to the measurements is found. In both cases, the main heat release takes place in phases $\Phi_3$ to $\Phi_5$. Also the flame shape and the lift off height is matched exactly for case 1. For case 2, the flame displays a slightly higher tendency to be detached from the injector as compared to the experiments but compared to case 1 a clear attachment trend is observed.

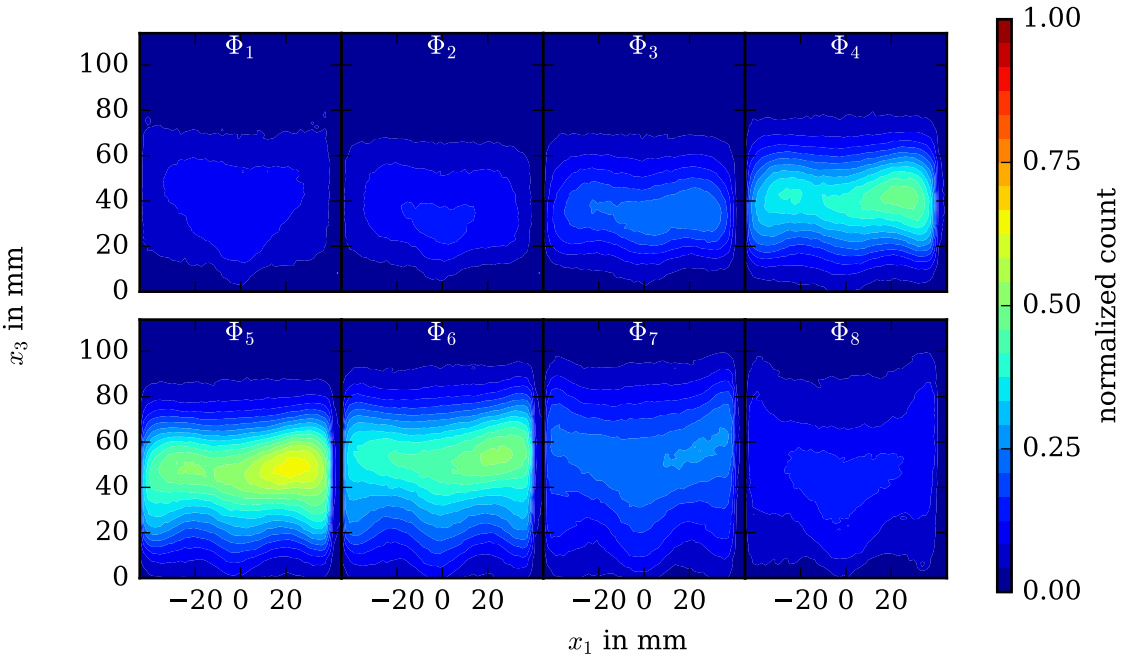


**Fig. 5 Phase averaged OH*-chemiluminescence measurements for case 1**

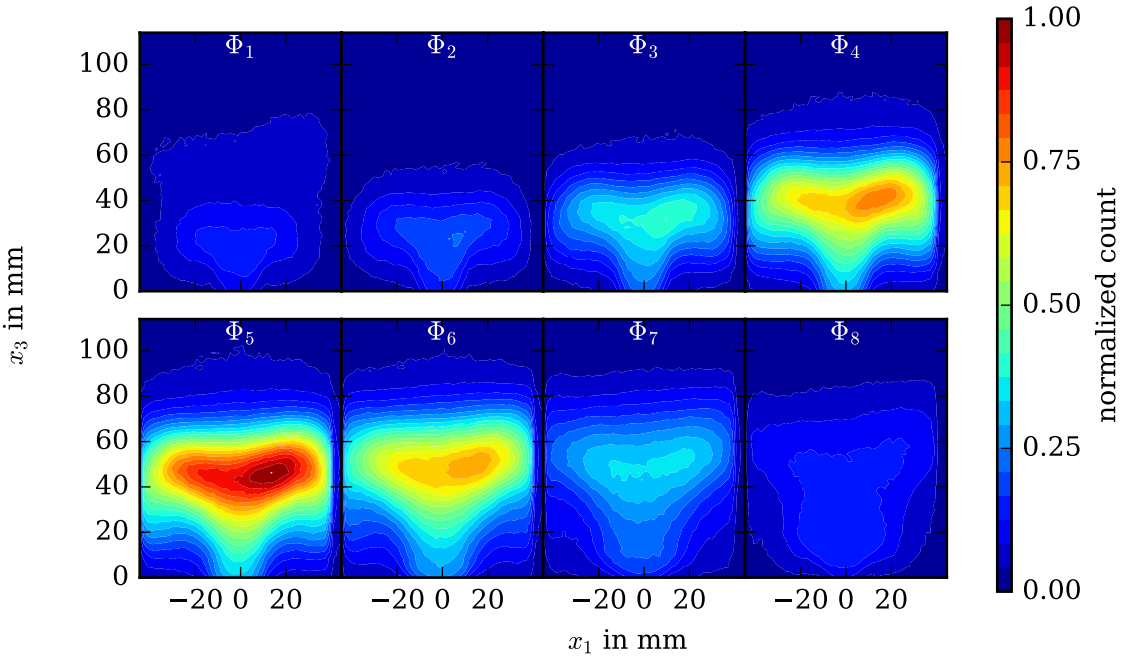


**Fig. 6 Phase averaged OH*-chemiluminescence measurements for case 2**

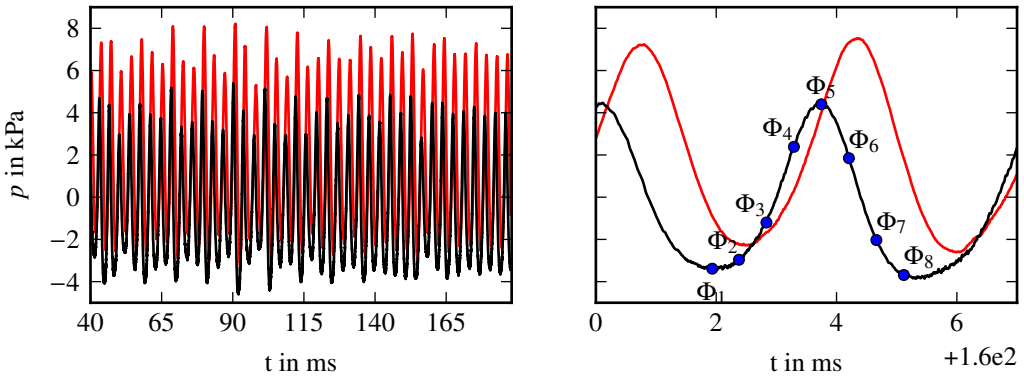


**Fig. 7 Selected time interval from the computed pressure signal of case 1. Pressure inside the air plenum (——), combustion chamber (——), and definition of phases ($\Phi_1$ to $\Phi_8$).**

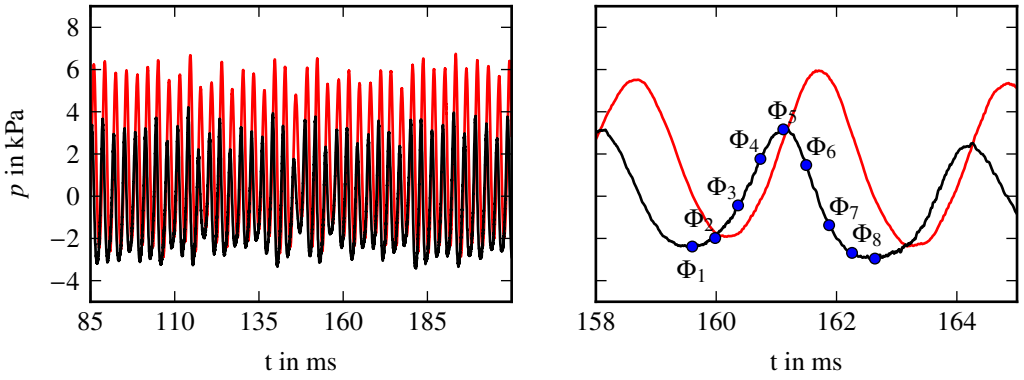


**Fig. 8 Selected time interval from the computed pressure signal of case 2. Pressure inside the air plenum (——), combustion chamber (——), and definition of phases ($\Phi_1$ to $\Phi_8$).**

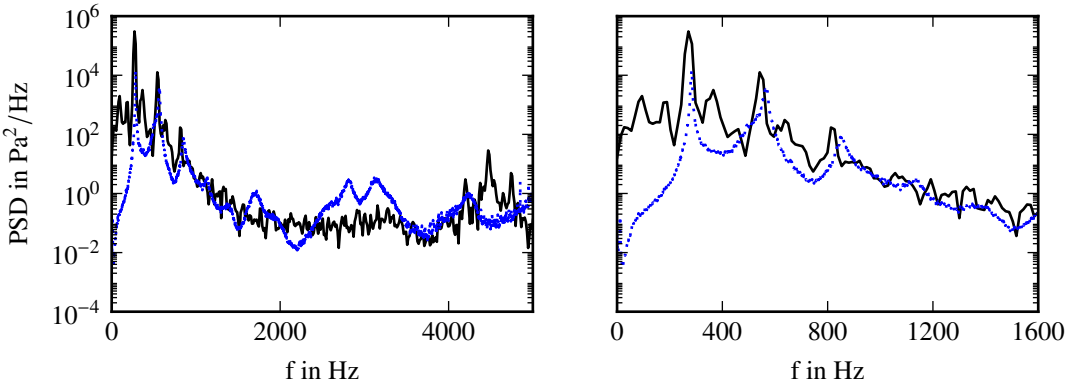


**Fig. 9 Comparison of the PSDs for case 1. ICS scheme (——). Measurements configuration A2 (——)**

*Thermoacoustic limit cycle*

The thermoacoustic oscillation cycle can be explained by considering the pressure history given in Fig. 7 in combination with the phase averaged heat release displayed in Fig. 11 and the phase averaged methane mass fraction

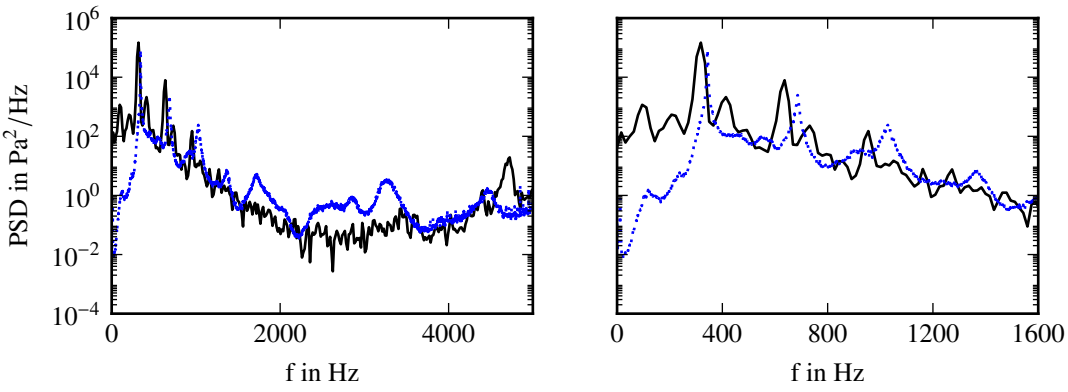


**Fig. 10 Comparison of the PSDs for case 2. ICS scheme (——). Measurements configuration A2 (——)**

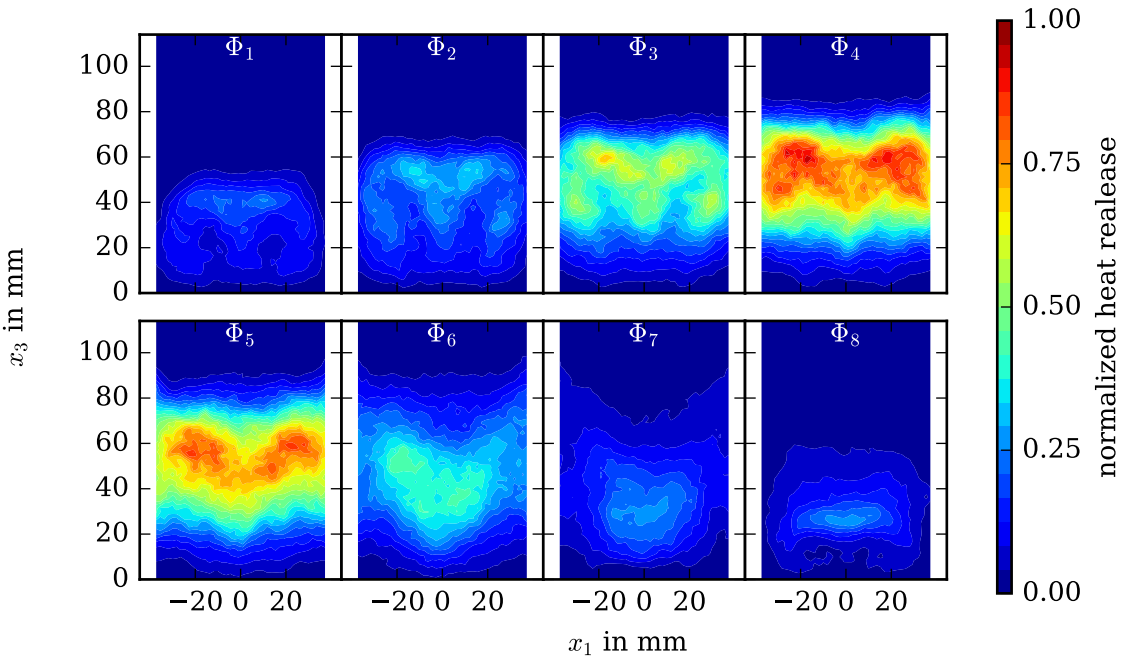


**Fig. 11 Phase averaged heat release for the computed case 1**

alongside the velocities shown in Fig. 13. Starting in phase $\Phi_1$ the pressure inside the combustion chamber is below the pressure inside the air plenum. As displayed in Fig. 13, this results in a a discharge of fuel rich gas into the combustion chamber. During this phase, the inner and outer recirculation zones are fully developed. In phase $\Phi_2$, the combustion processes increase in intensity and reach their peak during phases $\Phi_4$ and $\Phi_5$, as displayed in Fig. 11. Due to the increase in combustion intensity, the volumetric expansion of the gas leads to an increase in pressure inside the combustion chamber. For the phases $\Phi_3$ to $\Phi_5$ this results in a state, where the pressure inside the combustion chamber overshoots the pressure inside the air plenum (cf. Fig. 7). Consequently, the flow out of the injector becomes weaker and less fuel rich gas is transported into the combustion zone. In Fig. 13 phase $\Phi_5$, an actual flow reversal can be observed. This blockage effect of the flame also leads to an increase of pressure inside the air plenum. From phase $\Phi_5$ onward the pressure inside the air plenum is again higher than inside the combustion chamber and the flow from air plenum to

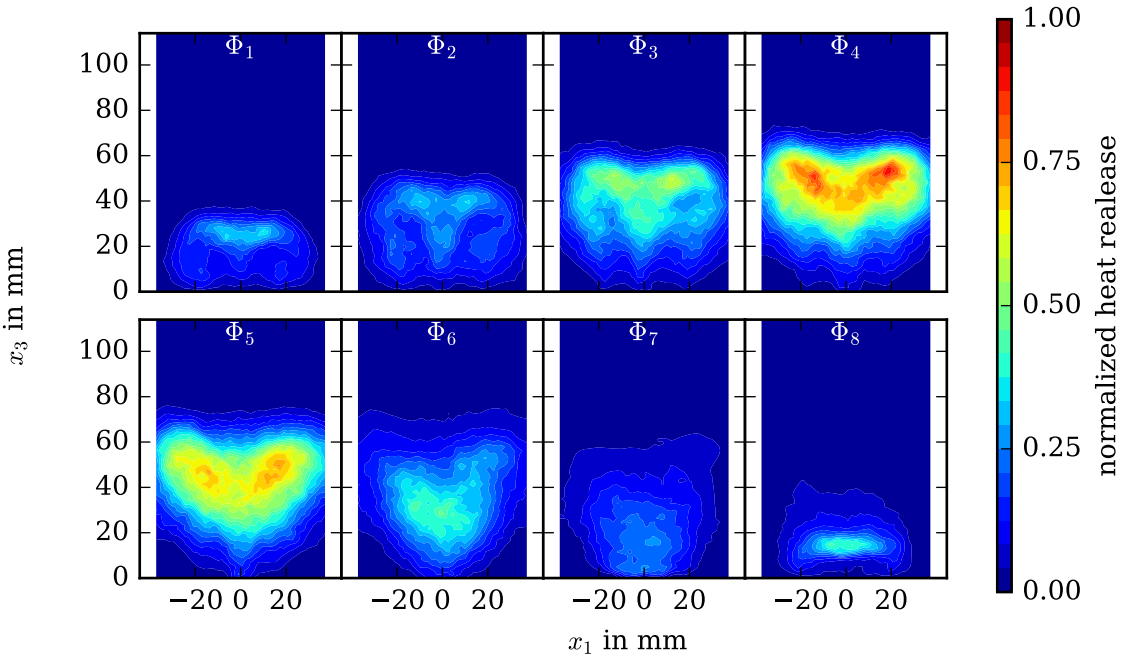


**Fig. 12 Phase averaged heat release for the computed case 2**

combustion chamber is again building up. At the same time, most of the fuel is consumed by combustion and due to the blockage effect no fresh fuel rich gas has entered the combustion chamber. Therefore, the flame intensity is decreasing. With phases $\Phi_7$ and $\Phi_8$ the recirculation zones begin to rebuild and fuel rich gas is again discharged into the combustion chamber. This leads to phase $\Phi_1$ and to a restart of the thermoacoustic cycle.

*Mode analysis*

The multiresolution proper orthogonal decomposition (MRPOD) of [79–81] is used to identify the thermoacoustic mode characteristics as well as coherent structures of the flow field. The MRPOD is used instead of the conventional proper orthogonal decomposition (POD) as the former has the ability to perform a POD for discrete frequency bands. The discrete frequency bands denoted by $I$ used for the analysis together with the PSD of the combustion chamber pressure as a reference are given in Fig. 14. Whereas, the MRPOD of a variable $\zeta(x_i,t)$ in the frequency band $I$ is denoted by

$$\zeta(x_i,t)'_I \quad = \quad \sum_{k=1}^{N} a_{k,I}(\zeta,t)\ \phi_{k,I}(\zeta,x_i), \tag{15}$$

with $N$ being the length of the time series, $a_{k,I}(\zeta,t)$ the $k$th temporal coefficient of the frequency band $I$, and $\phi_{k,I}(\zeta,x_i)$ the corresponding spatial mode. Further, $\zeta(x_i,t)'$ denotes the fluctuation and $\langle\ \zeta(x_i,t)\rangle$ the time average of the variable $\zeta(x_i,t)$, as in

$$\zeta(x_i,t) \quad = \quad \langle\zeta(x_i,t)\rangle + \zeta(x_i,t)'\ . \tag{16}$$

Performing the MRPOD for the frequency bands $I_1$ and $I_2$ of variables pressure $p$ and axial velocity $u_3$ the relative energy contents for the resulting modes are given in Fig. 15. Concerning the relative energy content of the MRPOD-modes for $p$ in the interval $I_1$ displayed by Fig. 15 it is clear, that only the modes $\phi_{1,I_1}(p)$ and $\phi_{2,I_1}(p)$ contribute to the oscillation observed for the first peak in Fig. 9. A slice through the central $x_1$-$x_3$-plane for the first two spatial MRPOD pressure modes in the frequency band $I_1$ for case 1 ($\phi_{1,I_1}(p)$ and $\phi_{2,I_1}(p)$) is displayed in Fig. 16. In addition, a profile of

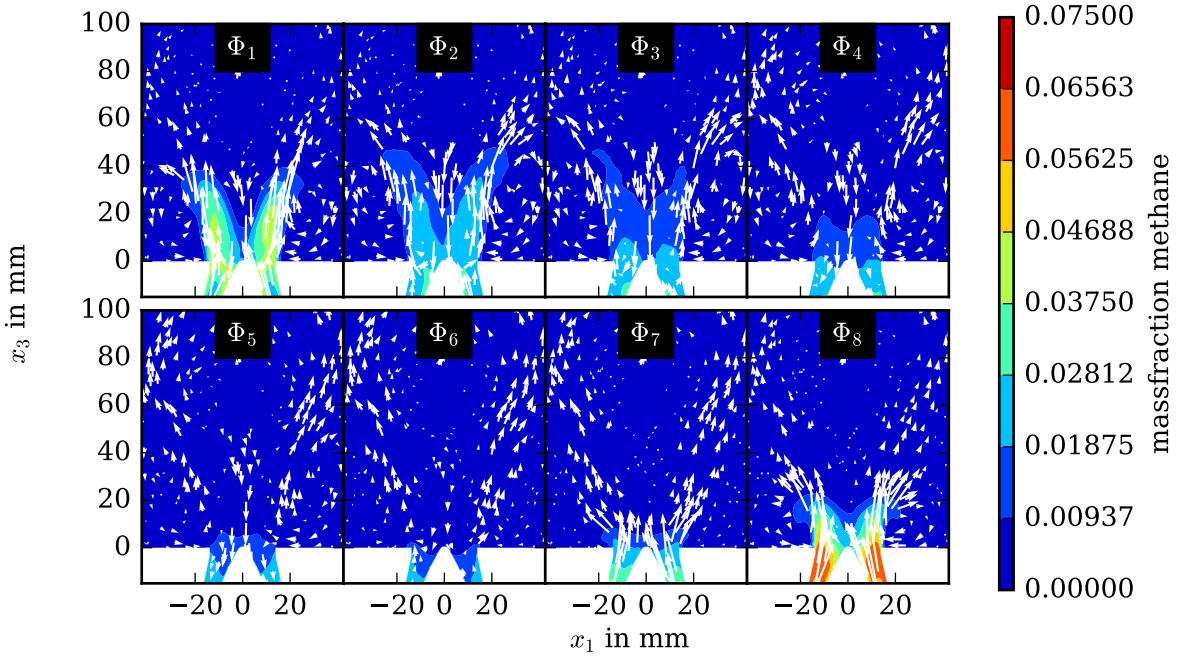


**Fig. 13 Phase averaged methane mass fraction (contours) and phase averaged velocity (vectors) for case 1.**

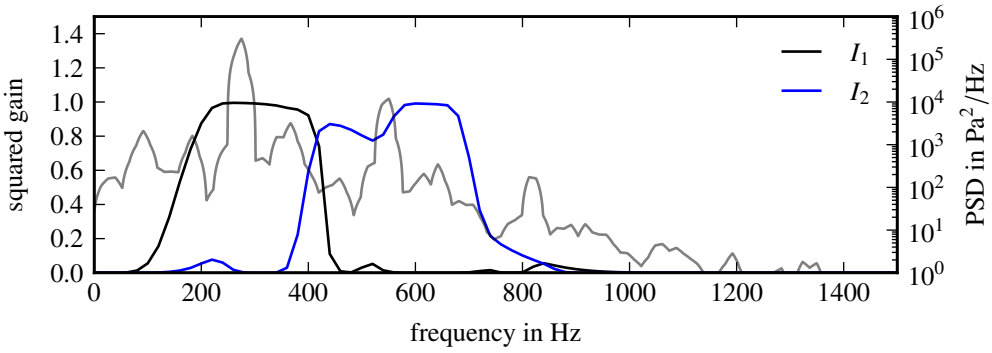


**Fig. 14 Squared gain of filters used for the MRPOD analysis.**

the spatial mode data extracted along a path through the combustion device is shown. The contour plot for the first mode $\phi_{1,I_1}(p)$ indicates no change perpendicular to the axial $x_3$-direction in the air plenum and large regions of the combustion chamber. The same can be observed for the second mode $\phi_{2,I_1}(p)$. This displays the longitudinal nature of the pressure oscillation observed for the first peak of Fig. 9. Further, by looking at the values along the path for mode $\phi_{1,I_1}(p)$ shows that the pressure inside the air plenum and the combustion chamber oscillates with the same phase for mode $\phi_{1,I_1}(p)$. The second spatial pressure mode $\phi_{2,I_1}(p)$ however, reveals that the pressure inside the air plenum and the combustion chamber oscillates out-of-phase for mode $\phi_{2,I_1}(p)$. Considering the pressure history of Fig. 7 a phase shift between the pressure inside the plenum and the chamber is observed. Under the observations made for $\phi_{1,I_1}(p)$ and $\phi_{2,I_1}(p)$ this implies, that an interplay of the MRPOD pressure modes $\phi_{1,I_1}(p)$ and $\phi_{2,I_1}(p)$ in the interval $I_1$ may be responsible for this phase shift as these modes are the most energetic contributors. Indeed, by using Eq. (15) to reconstruct $p'$ for the pressure inside the air plenum and the combustion chamber (i.e. using only spatial modes

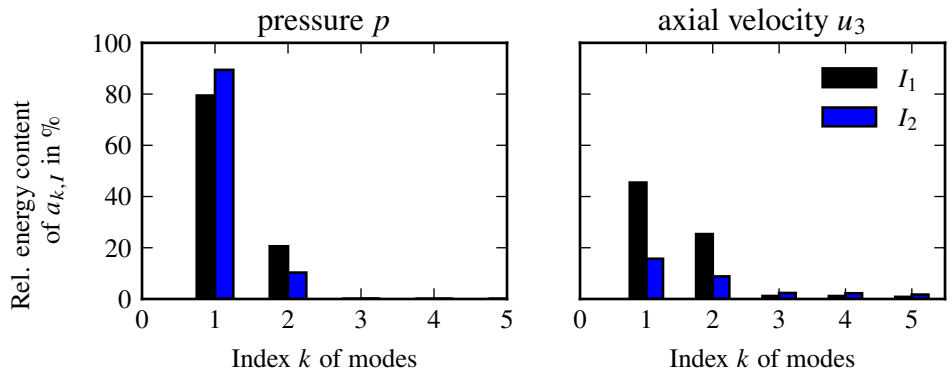


**Fig. 15 Relative energy content of the aquired MRPOD modes for case 1.**

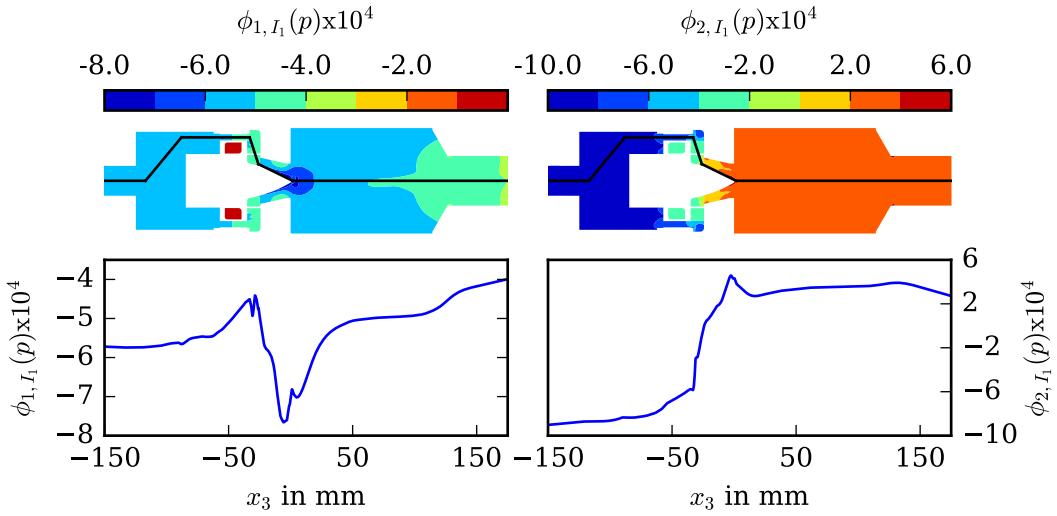


**Fig. 16 Spatial MRPOD pressure modes $\phi_{1,I_1}(p)$ and $\phi_{2,I_1}(p)$ for interval $I_1$ in $x_1$-$x_3$-plane (top) and extracted along the path (bottom) for case 1. The path is displayed in the contour plots by (——)**

$\phi_{1,I_1}(p)$, $\phi_{2,I_1}(p)$, and their respective temporal coefficients $a_{1,I_1}(p)$ and $a_{2,I_1}(p)$) a similar phase shift is obtained as displayed in Fig. 17. Further, this observation is backed by the experimental data where also such a phase shift can be observed (cf. Fig 2). Considering the relative energy contents for the MRPOD of the axial velocity in Fig. 15, again, most of the energy is accumulated in the first two modes ($\phi_{1,I_1}(u_3)$ and $\phi_{2,I_1}(u_3)$). Also for the second peak within the interval $I_2$, a large part is covered by $\phi_{1,I_2}(u_3)$ and $\phi_{2,I_2}(u_3)$. These first two modes are also found in the relative energy contents of the MRPOD pressure modes. It is therefore assumed that they are related to the acoustic oscillations. Further, the swirl burner is known to exhibit a PVC structure for certain operational points. The PVC is associated with a frequency within the frequency band $I_2$. Such a hydrodynamic structure is characterized by two modes of identical energy content as found for modes $\phi_{3,I_2}(u_3)$ and $\phi_{4,I_2}(u_3)$. As shown in Fig. 18 even though the energy content of $\phi_{3,I_2}(u_3)$ and $\phi_{4,I_2}(u_3)$ is marginal as compared to modes $\phi_{1,I_2}(u_3)$ and $\phi_{2,I_2}(u_3)$ a clear PVC structure is obtained. Whether the PVC is present throughout all phases of the thermoacoustic cycle as well as its influence on the thermoacoustic instabilities needs further clarification.

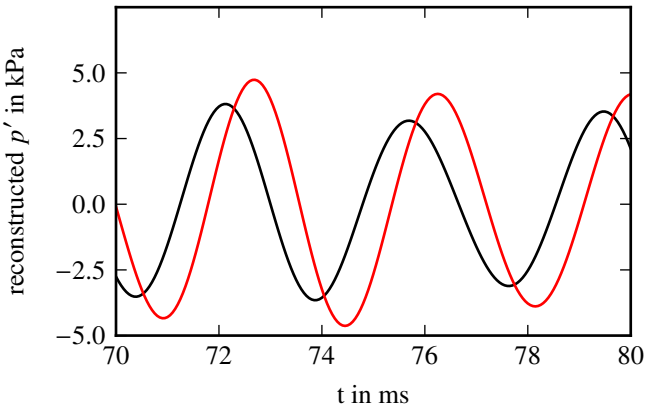


**Fig. 17 Selected time interval of the reconstructed pressure fluctuations for the first two MRPOD pressure modes of case 1. (——) combustion chamber. (——) air plenum**

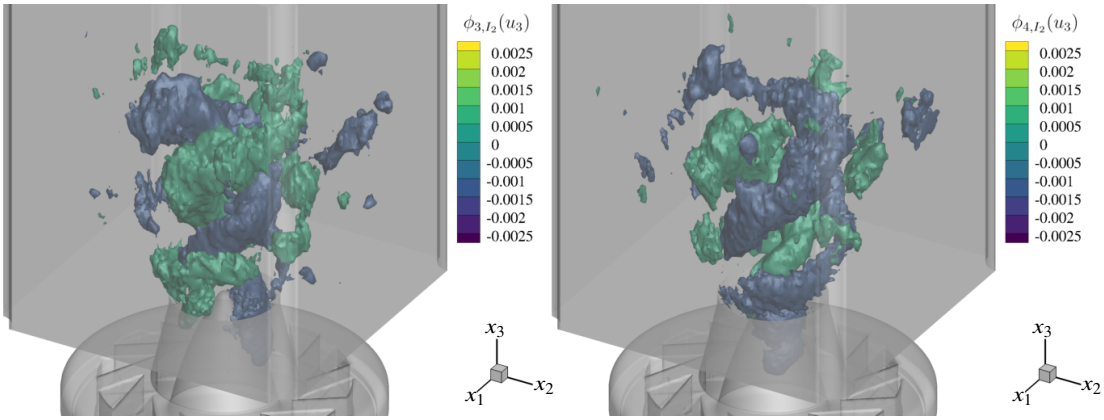


**Fig. 18 PVC structure in spatial MRPOD velocity modes $\phi_{3,I_2}(u_3)$ (left) and $\phi_{4,I_2}(u_3)$ (right).**

## VI. Summary and Conclusion

New measurement results for two lean partially premixed swirl flames with focus on reduction of acoustic and gaseous losses are presented. Therefore, pressure measurements are conducted using an stiff combustion chamber without optical access. Further, a combustion chamber providing a optical access at one side only is used for high speed OH*-chemiluminescence measurements in order to assess the spatial distribution of the heat release. Alongside the experimental efforts the cases are also investigated numerically using the recently proposed ICS-method. The findings can be summarized as follows:

- The application of the stiff combustion chamber (configuration A2) alongside the two-step calibration does not reveal any significant peaks at higher frequencies. Further, no increase in pressure amplitude is observed by the application of configuration A2 as compared to prior experiments utilizing sheet metal walls.
- Experimentally, for configuration A1 a detached flame is found for case 1 while for case 2 an attached flame is observed.
- The capabilities of the ICS-scheme computing self excited thermoacoustic instabilities is demonstrated. Concerning the frequencies of the excited pressure oscillations for the cases considered, excellent results are obtained compared to the experimental findings. However, the amplitudes are slightly overestimated by the simulations. In contrast, the spatial distribution of the phase averaged heat release is in a very good agreement compared to the OH*-chemiluminescence measurements. Therefore, the ICS-scheme is seen to be capable of computing self exited thermoacoustic combustion instabilities independent of operational conditions.
- Through the application of the MRPOD method it is revealed that the main thermoacoustic mode is driven by

a superposition of the two most energetic pressure modes inside the combustion chamber and the air plenum. Where the pressure mode with the highest energy leads to an in phase oscillation of air plenum and combustion chamber and the second most energetic mode leads to an out-of-phase oscillation.

- Finally, using the MRPOD method it is confirmed, that an PVC is present under the operational conditions of case 1.

## References


[1] Choi, D., and Merkle, C., "Application of time-iterative schemes to incompressible flow," *AIAA Journal*, Vol. 23, No. 10, 1985, pp. 1518–1524.

[2] Shuen, J.-S., Chen, K.-H., and Choi, Y., "A coupled implicit method for chemical non-equilibrium flows at all speeds," *Journal of Computational Physics*, Vol. 106, No. 2, 1993, p. 306–318.

[3] Withington, J. P., Shuen, J. S., and Yang, V., "A time accurate, implicit method for chemically reacting flows at all mach numbers," *29th Aerospace Sciences Meeting*, 1991.

[4] Pletcher, R. H., Tannehill, J. C., and Anderson, D. A., *Computational fluid mechanics and heat transfer*, CRC Press, 2012.

[5] Chen, K.-H., and Shuen, J.-S., "Three-dimensional coupled implicit methods for spray combustion flows at all speeds," *30th Joint Propulsion Conference and Exhibit*, 1994, pp. 1–19.

[6] Turkel, E., "Preconditioned methods for solving the incompressible and low speed compressible equations," *Journal of Computational Physics*, Vol. 72, No. 2, 1987, pp. 277–298.

[7] Turkel, E., "Review of preconditioning methods for fluid dynamics," *Applied Numerical Mathematics*, Vol. 12, No. 1, 1993, pp. 257–284. Special Issue.

[8] Choi, Y., and Merkle, C., "The application of preconditioning in viscous flows," *Journal of Computational Physics*, Vol. 105, 1993, pp. 207–223.

[9] van Leer, B., Lee, W., and Roe, P., "Characteristic time-stepping or local preconditioning of the euler equations," *10th Computational Fluid Dynamics Conference*, 1991, pp. 260–282.

[10] Weiss, J., and Smith, W., "Preconditioning applied to variable and constant density flows," *AIAA Journal*, Vol. 33, 1995, pp. 2050–2057.

[11] Briley, W., Taylor, L., and Whitfield, D., "High-resolution viscous flow simulations at arbitrary mach number," *Journal of Computational Physics*, Vol. 184, 2003, pp. 79–105.

[12] Rossow, C., "Efficient computation of compressible and incompressible flows," *Journal of Computational Physics*, Vol. 220, 2007, pp. 879–899.

[13] Colin, Y., Deniau, H., and Boussuge, J., "A robust low speed preconditioning formulation for viscous flow computations," *Computers and Fluids*, Vol. 47, 2011, pp. 1–15.

[14] Ferziger, J. H., and Perić, M., *Computational methods for fluid dynamics*, Springer, 2002.

[15] Demirdžić, I., Ž. Lilek, and Perić, M., "A collocated finite volume method for predicting flows at all speeds," *International Journal for Numerical Methods in Fluids*, Vol. 16, No. 12, 1993, pp. 1029–1050.

[16] Issa, R., Gosman, A., and Watkins, A., "The computation of compressible and incompressible recirculating flows by a non-iterative implicit scheme," *Journal of Computational Physics*, Vol. 62, 1986, pp. 66–82.

[17] Karki, K. C., and Patankar, S. V., "Pressure based calculation procedure for viscous flows at all speeds in arbitrary configurations," *AIAA Journal*, Vol. 27, No. 9, 1989, pp. 1167–1174.

[18] van Doormal, J. P., Raithby, G., and McDonald, B. H., "The segregated approach to predicting viscous compressible fluid flows," *Journal of Turbomachinery*, Vol. 109, No. 2, 1987, pp. 268–277.

[19] Shyy, W., Chen, M., and Sun, C., "Pressure-based multigrid algorithm for flow at all speeds," *AIAA Journal*, Vol. 30, 1992, pp. 2660–2669.

[20] Moukalled, F., and Darwish, M., "A high-resolution pressure-based algorithm for fluid flow at all speeds," *Journal of Computational Physics*, Vol. 168, 2001, pp. 101–130.

[21] Wall, C., Pierce, C. D., and Moin, P., "A semi-implicit method for resolution of acoustic waves in low mach number flows," *Journal of Computational Physics*, Vol. 181, No. 2, 2002, pp. 545–563.

[22] Xiao, C., Denner, F., and van Wachem, B., "Fully-coupled pressure-based finite-volume framework for the simulation of fluid flows at all speeds in complex geometries," *Journal of Computational Physics*, Vol. 346, 2017, pp. 91–130.

[23] Chorin, A. J., "On the convergence of discrete approximations to the navier-stokes equations," *Mathematics of Computation*, Vol. 23, No. 106, 1969, pp. 341–353.

[24] Strang, G., "On the construction and comparison of difference schemes," *SIAM Journal on Numerical Analysis*, Vol. 5, No. 3, 1968, pp. 506–517.

[25] Kim, J., and Moin, P., "Application of a fractional-step method to incompressible navier-stokes equations," *Journal of Computational Physics*, Vol. 59, No. 2, 1985, pp. 308–323.

[26] Moureau, V., Bérat, C., and Pitsch, H., "An efficient semi-implicit compressible solver for large-eddy simulations," *Journal of Computational Physics*, Vol. 226, No. 2, 2007, pp. 1256–1270.

[27] Yabe, T., and Wang, P.-Y., "Unified numerical procedure for compressible and incompressible fluid," *Journal of the Physical Society of Japan*, Vol. 60, No. 7, 1991, pp. 2105–2108.

[28] Yoon, S. Y., and Yabe, T., "The unified simulation for incompressible and compressible flow by the predictor-corrector scheme based on the CIP method," *Computer Physics Communications*, Vol. 119, No. 2, 1999, pp. 149–158.

[29] Kadioglu, S. Y., and Sussman, M., "Adaptive solution techniques for simulating underwater explosions and implosions," *Journal of Computational Physics*, Vol. 227, No. 3, 2008, pp. 2083–2104.

[30] Kitano, T., Kurose, R., and Komori, S., "Effects of internal pressure and inlet velocity disturbances of air and fuel droplets on spray combustion field," *Journal of Thermal Science and Technology*, Vol. 8, 2013, pp. 269–280.

[31] Kitano, T., Tsuji, T., Kurose, R., and Komori, S., "Effect of pressure oscillation on flashback characteristics in a turbulent channel flow," *Energy & Fuels*, Vol. 29, No. 10, 2015, pp. 6815–6822.

[32] Roy, R. N., Muto, M., and Kurose, R., "Direct numerical simulation of ignition of syngas ($H_2$/CO) mixtures with temperature and composition stratifications relevant to HCCI conditions," *International Journal of Hydrogen Energy*, Vol. 42, No. 41, 2017, pp. 26152–26161.

[33] Ahmed, U., Pillai, A., Chakraborty, N., and Kurose, R., "Statistical behavior of turbulent kinetic energy transport in boundary layer flashback of hydrogen-rich premixed combustion," *Phys. Rev. Fluids*, Vol. 4, 2019, p. 103201.

[34] Yu, P., Watanabe, H., Zhang, W., Kurose, R., and Kitagawa, T., "Flamelet model for a three-feed non-premixed combustion system with a diluent stream: Analysis and validation of quasi-two-dimensional flamelet (Q2DF) models," *Energy & Fuels*, Vol. 33, No. 5, 2019, pp. 4640–4650.

[35] Kai, R., Takahashi, A., and Kurose, R., "Numerical investigations of C1-C3 alkanes and H2 premixed flame-wall interaction: Effectiveness of insulation wall on heat loss reduction," *Journal of Thermal Science and Technology*, Vol. 15, No. 3, 2020, pp. 1–11.

[36] Ahmed, U., Pillai, A. L., Chakraborty, N., and Kurose, R., "Surface density function evolution and the influence of strain rates during turbulent boundary layer flashback of hydrogen-rich premixed combustion," *Physics of Fluids*, Vol. 32, No. 5, 2020, p. 055112.

[37] Konishi, K., Kai, R., and Kurose, R., "Unsteady flamelet modeling for N2H4/N2O4 flame accompanied by hypergolic ignition and thermal decomposition," *Applications in Energy and Combustion Science*, Vol. 5, 2021, p. 100022.

[38] Shehab, H., Watanabe, H., Minamoto, Y., Kurose, R., and Kitagawa, T., "Morphology and structure of spherically propagating premixed turbulent hydrogen - air flames," *Combustion and Flame*, Vol. 238, 2022, p. 111888.

[39] Kitano, T., Kaneko, K., Kurose, R., and Komori, S., "Large-eddy simulations of gas- and liquid-fueled combustion instabilities in back-step flows," *Combustion and Flame*, Vol. 170, 2016, pp. 63–78.

[40] Pillai, A. L., and Kurose, R., "Numerical investigation of combustion noise in an open turbulent spray flame," *Applied Acoustics*, Vol. 133, 2018, pp. 16–27.

[41] Nagao, J., Pillai, A. L., and Kurose, R., "Investigation of temporal variation of combustion instability intensity in a back step combustor using LES," *Journal of Thermal Science and Technology*, Vol. 15, No. 3, 2020, p. JTST0036.

[42] Pillai, A. L., Nagao, J., Awane, R., and Kurose, R., "Influences of liquid fuel atomization and flow rate fluctuations on spray combustion instabilities in a backward-facing step combustor," *Combustion and Flame*, Vol. 220, 2020, pp. 337–356.

[43] Pillai, A. L., and Kurose, R., "Combustion noise analysis of a turbulent spray flame using a hybrid DNS/APE-RF approach," *Combustion and Flame*, Vol. 200, 2019, pp. 168–191.

[44] Pillai, A. L., Inoue, S., Shoji, T., Tachibana, S., Yokomori, T., and Kurose, R., "Investigation of combustion noise generated by an open lean-premixed H2/air low-swirl flame using the hybrid LES/APE-RF framework," *Combustion and Flame*, Vol. 245, 2022, p. 112360. doi:https://doi.org/10.1016/j.combustflame.2022.112360.

[45] Lourier, J.-M., Stöhr, M., Noll, B., Werner, S., and Fiolitakis, A., "Scale adaptive simulation of a thermoacoustic instability in a partially premixed lean swirl combustor," *Combustion and Flame*, Vol. 183, 2017, pp. 343–357.

[46] Grimm, F., Lourier, J.-M., Lammel, O., Noll, B., and Aigner, M., "A selective fast fourier filtering approach applied to high frequency thermoacoustic instability analysis," *Conference proceedings Turbo Expo: Power for Land, Sea, and Air*, Vol. Volume 4A: Combustion, Fuels and Emissions, 2017, pp. 1–14.

[47] Pries, M., Fiolitakis, A., and Gerlinger, P., "An implicit splitting scheme with characteristic boundary conditions for compressible reactive flows on unstructured grids," *Journal of Computational and Applied Mathematics*, Vol. 437, 2024, p. 115446.

[48] Weigand, P., Duan, X. R., Meier, W., Meier, U., Aigner, M., and Bérat, C., "Experimental investigations of an oscillating lean premixed $CH_4$/air swirl flame in a gas turbine model combustor," *Proceedings of the European Combustion Meeting 2005*, 2005.

[49] Weigand, P., Meier, W., Duan, X., and Aigner, M., "Laser-based investigations of thermoacoustic instabilities in a lean premixed gas turbine model combustor," *Journal of Engineering for Gas Turbines and Power*, Vol. 129, No. 3, 2006, pp. 664–671.

[50] Meier, W., Weigand, P., Duan, X., and Giezendanner-Thoben, R., "Detailed characterization of the dynamics of thermoacoustic pulsation in a lean premixed swirl flame," *Combustion and Flame*, Vol. 150, No. 1, 2007, pp. 2–26.

[51] Arndt, C., Steinberg, A. M., Boxx, I. G., Meier, W., Aigner, M., and Carter, C. D., "Flow-field and flame dynamics of a gas turbine model combustor during transition between thermo-acoustically stable and unstable states," *Conference proceedings Turbo Expo: Power for Land, Sea, and Air*, Vol. Volume 2: Combustion, Fuels and Emissions, Parts A and B, 2010, pp. 677–687.

[52] Boxx, I., Arndt, C. M., Carter, C. D., and Meier, W., "High-speed laser diagnostics for the study of flame dynamics in a lean premixed gas turbine model combustor," *Experiments in Fluids*, Vol. 52, 2012, pp. 555–567.

[53] Steinberg, A., Arndt, C., and Meier, W., "Parametric study of vortex structures and their dynamics in swirl-stabilized combustion," *Proceedings of the Combustion Institute*, Vol. 34, No. 2, 2013, pp. 3117–3125.

[54] Oberleithner, K., Stöhr, M., Im, S. H., Arndt, C. M., and Steinberg, A. M., "Formation and flame-induced suppression of the precessing vortex core in a swirl combustor: Experiments and linear stability analysis," *Combustion and Flame*, Vol. 162, No. 8, 2015, pp. 3100–3114.

[55] Dem, C., Stöhr, M., Arndt, C. M., Steinberg, A. M., and Meier, W., "Experimental study of turbulence-chemistry interactions in perfectly and partially premixed confined swirl flames," *Zeitschrift für Physikalische Chemie*, Vol. 229, No. 4, 2015, pp. 569–595.

[56] Chong, L. T. W., Komarek, T., Kaess, R., Föller, S., and Polifke, W., "Indentification of flame transfer functions form LES of a premixed swirl burner," *Conference proceedings Turbo Expo: Power for Land, Sea, and Air*, Vol. Volume 2: Combustion, Fuels and Emissions, Parts A and B, 2010, pp. 623–635.

[57] Eder, A. J., Silva, C. F., M-Haeringer, Kuhlmann, J., and Polifke, W., "Incompressible versus compressible large eddy simulation for the identification of premixed flame dynamics," *International Journal of Spray and Combustion Dynamics*, Vol. 15, No. 1, 2023, pp. 16–32.

[58] Ghani, A., Poinsot, T., Gicquel, L., and Müller, J.-D., "LES study of transverse acoustic instabilities in a swirled kerosene/air combustion chamber," *Flow, Turbulence and Combustion*, Vol. 96, 2016, pp. 207–226.

[59] Franzelli, B., Riber, E., Gicquel, L. Y. M., and Poinsot, T., "Large Eddy Simulation of combustion instabilities in a lean partially premixed swirled flame," *Combustion and Flame*, Vol. 159, No. 2, 2012, pp. 621–637.

[60] Lourier, J.-M., Noll, B., and Aigner, M., "Extension of a compressible pressure-based solver for reacting flows," *19th AIAA/CEAS Aeroacoustics Conference*, 2013, pp. 1–13.

[61] Lourier, J.-M., Noll, B., and Aigner, M., "Large eddy simulaiton of a thermoacoustic instability within a swirl-stabilzed burner using impedance boundary conditions," *Proceedings of ASME Turbo Expo 2014: Turbine Technical Conference and Exposition*, 2014, pp. 1–12.

[62] Lourier, J.-M., Eberle, C., Noll, B., and Aigner, M., "Influence of turbulence-chemistry interaction modeling on the structure and the stability of a swirl-stabilized flame," *Proceedings of ASME Turbo Expo 2015: Turbine Technical Conference and Exposition*, 2015, pp. 1–12.

[63] Volpiani, P. S., Schmitt, T., and Veynante, D., "Large eddy simulation of a turbulent swirling premixed flame coupling the TFLES model with a dynamic wrinkling formulation," *Combustion and FlamCombustion and Flame*, Vol. 180, 2017, pp. 124–135.

[64] Fredrich, D., Jones, W. P., and Marquis, A. J., "A combined oscillation cycle involving self-excited thermo-acoustic and hydrodynamic instability mechanisms," *Physics of Fluids*, Vol. 33, No. 8, 2021, p. 085122.

[65] Fredrich, D., Jones, W. P., and Marquis, A. J., "Thermo-acoustic instabilities in the PRECCINSTA combustor investigated using a compressible LES-pdf approach," *Flow, Turbulence and Combustion*, Vol. 106, 2021, pp. 1399–1415.

[66] Zhao, S., Bhairapurada, K., Tayyab, M., Mercier, R., and Boivin, P., "Lattice-Boltzmann modeling of the quiet and unstable PRECCINSTA burner modes," *Computers & Fluids*, Vol. 260, 2023, p. 105898.

[67] Gövert, S., Lipkowicz, J. T., and Janus, B., "Compressible large eddy simulations of thermoacoustic instabilities in the preccinsta combustor using flamelet generated manifolds with dynamic thickened flame model," *Proceedings of the ASME Turbo Expo 2023*, 2023, pp. 1–15.

[68] Venkatakrishnan, V., *On the accuracy of limiters and convergence to steady state solutions*, 1993.

[69] dos Santos, F. L., Botero-Bolívar, L., Venner, C. H., and de Santana, L. D., "Analysis of the remote microphone probe technique for the determination of turbulence quantities," *Applied Acoustics*, Vol. 208, 2023, p. 109387.

[70] Botero-Bolívar, L., dos Santos, F. L., Venner, C. H., and de Santana, L. D., "Study of the development of a boundary layer using the remote microphone probe technique," *Experiments in Fluids*, Vol. 64, No. 88, 2023.

[71] de Wyer, N. V., Zapata, A., Nogueria, D., and Schram, C., "Development of a test rig for the measurement of turbulent boundary layer wall pressure statistics," *2018 AIAA/CEAS Aeroacoustics Conference*, 2018, pp. 1–19.

[72] Poinsot, T., and Lele, S., "Boundary conditions for direct simulations of compressible viscous flows," *Journal of Computational Physics*, Vol. 101, No. 1, 1992, pp. 104–129.

[73] Rudy, D. H., and Strikwerda, J. C., "A nonreflecting outflow boundary condition for subsonic navier-stokes calculations," *Journal of Computational Physics*, Vol. 36, No. 1, 1980, pp. 55–70.

[74] Yin, Z., Nau, P., and Meier, W., "Responses of combustor surface temperature to flame shape transitions in a turbulent bi-stable swirl flame," *Experimental Thermal and Fluid Science*, Vol. 82, 2017, pp. 50–57.

[75] Arndt, C. M., Nau, P., and Meier, W., "Characterization of wall temperature distributions in a gas turbine model combustor measured by 2D phosphor thermometry," *Proceedings of the Combustion Institute*, Vol. 38, No. 1, 2021, pp. 1867–1875.

[76] Kazakov, A., and Frenklach, M., "Reduced reaction set based on GRI-mech 1.2," , 2024. URL `http://www.me.berkeley.edu/drm/`.

[77] Nicoud, F., and Ducros, F., "Subgrid-scale stress modelling based on the square of the velocity gradient tensor," *Flow, Turbulence and Combustion*, Vol. 62, 1999, pp. 183–200.

[78] Gerlinger, P., Möbus, H., and Brüggemann, D., "An Implicit Multigrid Method for Turbulent Combustion," *Journal of Computational Physics*, Vol. 167, No. 2, 2001, pp. 247–276.

[79] Yin, Z., and Stöhr, M., "Time–frequency localisation of intermittent dynamics in a bistable turbulent swirl flame," *Journal of Fluid Mechanics*, Vol. 882, 2020, p. A30.

[80] Grader, M., Yin, Z., Geigle, K. P., and Gerlinger, P., "Influence of flow field dynamics on soot evolution in an aero-engine model combustor," *Proceedings of the Combustion Institute*, Vol. 38, No. 4, 2021, pp. 6421–6429.

[81] Grader, M., and Gerlinger, P., "Influence of operating conditions on flow field dynamics and soot formation in an aero-engine model combustor," *Combustion and Flame*, Vol. 258, 2023, p. 112712. Special issue and Perspective on the Chemistry and Physics of Carbonaceious Particle Formation.